ACS OMEGA

Open Access

http://pubs.acs.org/journal/acsodf

Article

Studies on Photocatalytic and Antioxidant Efficacy of Ag-Embedded ZnO Nanocomposites

Sachin K. Dhawale, Prashant D. Sarvalkar, Chetan S. Shinde, Neeraj R. Prasad, Kalyanrao M. Garadkar, Kiran Kumar K. Sharma, and Avinash A. Ramteke*

Cite This: *ACS Omega* 2025, 10, 11948−11960

Read Online

ACCESS | Metrics & More | Article Recommendations | Supporting Information

ABSTRACT: This study focuses on the synthesis and characterization of Ag-embedded ZnO nanocomposites with varying silver (Ag) contents (1, 3, and 5 wt %) to evaluate their photocatalytic and antioxidant activities. The nanocomposites were synthesized using a sol−gel method, followed by thermal decomposition, and characterized by XRD, SEM, BET, Raman, EDS, TEM, FTIR, and UV−vis spectroscopy. The photocatalytic degradation of the rhodamine 6G (R6G) dye was tested under UV light, and its antioxidant capacity was evaluated using DPPH, ABTS, FRAP, and FIC assays. Among the synthesized samples, the ZnO-5 wt % Ag nanocomposite exhibited the enhanced photocatalytic efficiency, achieving 93.36% degradation of R6G, with a reaction rate constant of 6.54×10^{-3} min^{-1}. It also demonstrated recyclability, retaining over 91% efficiency after five cycles. In the antioxidant assays, the ZnO-5 wt % Ag composite showed enhanced free radical scavenging capacity, confirming its strong antioxidant potential. These Ag-embedded ZnO nanocomposites offer a dual functionality, enhancing both photocatalytic and antioxidant activities. Future research will focus on their scalability and visible-light photocatalytic performance to enhance their applications in environmental remediation and biomedical applications.

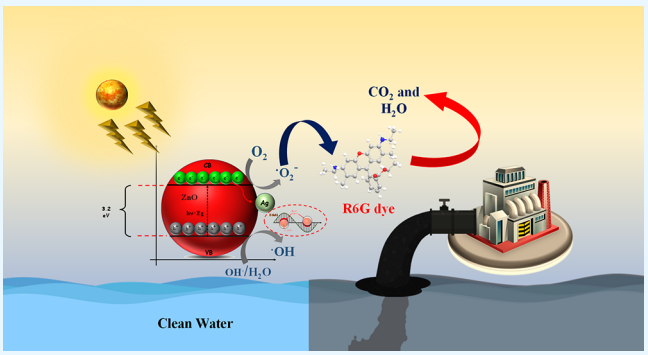

1. INTRODUCTION

Nanomaterials, particularly metal oxide-based nanocomposites, have gained significant attention owing to their unique physicochemical properties such as high surface area, tunable band gaps, and enhanced reactivity, which enable a wide range of applications, viz., catalysis,[1] environmental remediation,[2] biomedicine,[3,4] textiles, energy storage devices, sensors,[5] etc. Among these, zinc oxide (ZnO) nanoparticles (NPs) are of particular interest because of their exceptional photocatalytic activity, high chemical stability, and biocompatibility.[6] ZnO NPs have a wide band gap (3.2 eV), which allows them to absorb UV light and efficiently generate reactive oxygen species (ROS), such as hydroxyl radicals (•OH) and superoxide anions ($\bullet O_2^-$), making them highly effective for the photocatalytic degradation of various organic pollutants, including dyes, pharmaceuticals, and industrial effluents.[7−10]

In recent studies, ZnO-based photocatalysts have demonstrated degradation efficiencies ranging from 80 to 95% for organic pollutants, such as rhodamine 6G (R6G) and methylene blue (MB), under UV irradiation.[11−14] However, a key challenge is the rapid recombination of photogenerated electron−hole pairs, which significantly reduces the overall photocatalytic efficiency.[6] This recombination can reduce the quantum efficiency of photocatalytic processes by as much as 50−60%, hindering the long-term application of ZnO-based photocatalysts in real-world scenarios.[15]

To overcome this limitation and enhance photocatalytic performance, the incorporation of silver nanoparticles (Ag NPs) into ZnO has been extensively explored.[14] Ag NPs not only enhance charge separation by acting as electron acceptors but also introduce a localized surface plasmon resonance (LSPR) effect.[6] The LSPR effect is particularly prominent under visible light, where Ag NPs absorb light and induce electron oscillations at their surfaces, leading to enhanced light absorption and localized heating.[15,16] This effect improves photogenerated electron−hole separation and increases ROS production, thereby enhancing the photocatalytic efficiency under both UV and visible light.[16]

Incorporating Ag into ZnO has been shown to improve the photocatalytic activity by 20−40% compared to pure ZnO.[14] This significant enhancement in photocatalytic performance is largely attributed to the synergy between ZnO and Ag, where

Received: September 29, 2024
Revised: March 6, 2025
Accepted: March 12, 2025
Published: March 20, 2025

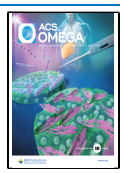

https://doi.org/10.1021/acsomega.4c08896
ACS Omega 2025, 10, 11948−11960

Ag NPs improve the absorption of visible light and increase the production of reactive oxygen species (ROS), such as superoxide radicals ($\bullet O_2^-$) and hydroxyl radicals ($\bullet OH$), which are key to breaking down organic pollutants.[17] Moreover, Ag NPs confer strong antimicrobial properties, which when combined with the photocatalytic activity of ZnO, provide a dual functionality in a single material. This dual functionality makes Ag-embedded ZnO nanocomposites not only effective for environmental decontamination but also highly promising for biomedical applications.[18,19]

In addition to their antimicrobial activity, Ag-embedded ZnO nanocomposites exhibit significant antioxidant activity, making them potential candidates for addressing oxidative stress-related diseases.[20−22] This antioxidant potential is critical for biomedical applications, particularly in the treatment of conditions related to oxidative damage, such as cancer, aging, and neurodegenerative diseases, such as Alzheimer's and Parkinson's.

This study focuses on the synthesis of Ag-embedded ZnO nanocomposites using a sol−gel method followed by thermal decomposition to optimize the incorporation of Ag and enhance both the photocatalytic and antioxidant properties of ZnO. The photocatalytic performance was evaluated by studying the degradation of the R6G dye, and the antioxidant capacity was assessed using a 2,2-diphenyl-1-picrylhydrazyl (DPPH) assay, a 2,2′-azinobis-3-ethylbenzothiazoline-6-sulfonic acid (ABTS) assay, a ferric reducing antioxidant power (FRAP) assay, and a ferrous ion chelating (FIC) assay. The results demonstrate that Ag incorporation significantly enhances both the photocatalytic efficiency and the antioxidant activity, positioning Ag-embedded ZnO nanocomposites as promising candidates for both environmental remediation and biomedical applications.

2. METHODOLOGIES

2.1. Chemicals. Analytical-grade chemicals were used as received without further purification. These included zinc acetate dihydrate [$Zn(CH_3COO)_2{\cdot}2H_2O$], sodium hydroxide (NaOH) (SD Fine Chemical Ltd.), and cetyltrimethylammonium bromide (Loba Chemie Pvt. Ltd.), and silver nitrate ($AgNO_3$) (AJAX Chemicals Timbi). Hydrogen peroxide (H_2O_2) was procured from Oswal Chemicals, Pune, and rhodamine 6G (R6G) was obtained from Fischer Scientific. Other reagents such as 2,4,6-tri-(2-pyridyl)-5-triazine (TPTZ), 2,2′-azinobis(3-ethylbenzothiazoline-6-sulfonic acid) (ABTS), 2,2-diphenyl-1-picrylhydrazyl (DPPH), ethanol, ferric chloride hexahydrate ($FeCl_3{\cdot}6H_2O$), ferrous sulfate heptahydrate ($FeSO_4{\cdot}7H_2O$), methanol, potassium persulfate, ferrozine, acetic acid, sodium acetate, ascorbic acid, and ethylenediaminetetraacetic acid (EDTA) were purchased from Sigma-Aldrich (Bangalore, India).

2.2. Synthesis of ZnO NPs. ZnO NPs were synthesized using the sol−gel method, as reported by Kassim et al.[23] In this experiment, 2.195 g of zinc acetate dihydrate was dissolved in 100 mL of ethanol and mixed with 2 mL of H_2O_2 to obtain a clear solution. CTAB (1 mM) was added to ethanol as the capping agent. A 0.4 M NaOH solution (25 mL), acting as a hydrolyzing agent, was prepared separately and added dropwise to the solution under constant stirring (∼900 rpm) for approximately 3 h. After complete addition, a sol was formed. The solution was then incubated overnight to form a gel. The gel was then dried at 110 °C in an oven for 2 h to convert it to $Zn(OH)_2$. The powder was then calcined at 800 °C for 4 h to obtain ZnO NPs.

2.3. Synthesis of Ag-Embedded ZnO Nanocomposites by a Thermal Decomposition Reaction. The process commenced with the synthesis of ZnO NPs by using the sol−gel method, as previously described. The $Zn(OH)_2$ powder was homogeneously mixed with $AgNO_3$ at varying concentrations (1, 3, and 5% w/w relative to $Zn(OH)_2$) using a mortar and pestle to ensure an even distribution of silver ions throughout $Zn(OH)_2$. The mixture was then thoroughly ground for 3 h to achieve uniformity. Subsequently, the composite powders were annealed at 800 °C for 4 h, promoting the incorporation of Ag into the ZnO. This resulted in the formation of Ag-embedded ZnO nanocomposites, labeled ZnO-1 wt % Ag, ZnO-3 wt % Ag, and ZnO-5 wt % Ag, based on the different silver concentrations integrated into the ZnO structure. Scheme S1 shows a schematic representation of the synthesis process for the Ag-embedded ZnO nanocomposites via thermal decomposition. The synthesized nanocomposites were stored for further characterization and potential applications.

2.4. Material Characterization. The crystallinity of the samples was assessed by powder XRD on a Rigaku Ultima IV diffractometer with a Cu Kα (λ = 1.54 Å) radiation source, scanning between 2θ values of 20 and 80° at a rate of 5°/min. The UV−visible absorption spectra of the dye solutions were recorded by using a Shimadzu UV-3600 spectrophotometer, and the synthesized nanomaterials were analyzed by using a Shimadzu UV-800 spectrophotometer to explore their optical properties. The surface morphology was characterized via scanning electron microscopy (SEM) using a Hitachi S3400N instrument. TEM was performed by using a JEOL JEM 2100 Plus instrument to investigate the morphological characteristics of the nanomaterials. The specific surface areas of the samples were measured using the Brunauer−Emmett−Teller (BET) method on a Quantachrome NOVA1000e instrument. Fourier-transform infrared (FTIR) spectra were obtained by using a Bruker Platinum ATR spectrometer to analyze the functional groups. Raman spectroscopy was conducted using a Renishaw Raman spectrometer over a spectral range of 200−800 cm^{-1} to identify vibrational modes and confirm the structural properties of the nanomaterials.

2.5. Photocatalytic Activity. We evaluated the photocatalytic activity of Ag-embedded ZnO nanocomposites by monitoring the degradation of R6G under UV light. In this study, 50 mg of the photocatalyst was dispersed in a reactor containing 100 mL of a 10 mM R6G solution. A magnetic stirrer ensured continuous mixing, while a high-pressure mercury vapor UV lamp (125 W, Philips) with 30.1 W/m^2 irradiance provided the UV light source, which was placed 2 cm away from the dye solution. The reactor temperature was controlled by using a cooling-water jacket. Prior to UV exposure, the mixture was stirred in the dark for 90 min to achieve an adsorption−desorption equilibrium of the dye and photocatalyst. The reaction mixture was then exposed to UV light with constant stirring to maintain a uniform suspension. Samples were centrifuged to separate the catalysts, and the supernatant was analyzed using UV−visible spectrophotometry at 526 nm to determine the residual R6G concentration.[14] The percentage degradation of R6G was calculated by assessing the photocatalytic efficiency of the nanocomposites using eq 1:

https://doi.org/10.1021/acsomega.4c08896
ACS Omega 2025, 10, 11948−11960

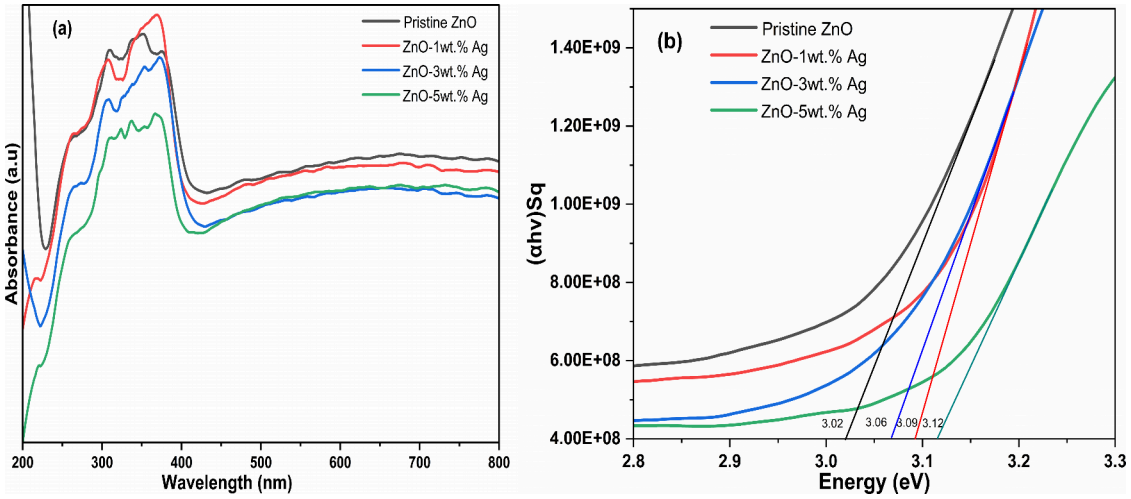

Figure 1. (a) UV−vis absorbance spectra and (b) Tauc's plot of ZnO NPs and Ag-ZnO nanocomposites.

$$\text{activity/degradation efficiency (\%)} = \frac{A_0 - A_t}{A_0} \times 100 \quad (1)$$

where A_o represents the initial absorbance of the sample and A_t represents the absorbance of sample at time *t*.

2.6. Evaluation of the Oxidative Stress Potential of Nanocomposites. *2.6.1. Assessment of Radical Scavenging Activity. 2.6.1.1. DPPH.* The antioxidant potential of the synthesized nanomaterials was evaluated *in vitro* using a modified DPPH assay[24] originally introduced by Brand-Williams et al.[25] This assay is widely used because of its simplicity and its reliance on the color change of the DPPH reagent from deep purple upon reduction. The percentage of DPPH radical scavenging activity (RSA) was calculated using eq 1, based on absorbance measurements taken at 517 nm using a UV−vis spectrophotometer.

2.6.1.2. ABTS. For the analysis of ABTS radical scavenging activity, 200 μL of the Ag-embedded ZnO nanocomposite and ZnO NP dispersed solutions was mixed with 2800 μL of ABTS solution. The ABTS working solution was prepared by mixing equal volumes (1:1) of a 7 mM ABTS aqueous solution and a 2.45 mM potassium persulfate solution, followed by incubation in the dark for 24 h to formation of ABTS radical cations. Subsequently, the reagent was diluted to obtain an absorbance of ∼1 (O.D.) at a wavelength of 734 nm. After completion of the reaction, the mixture was allowed to stand undisturbed at room temperature for 10 min to ensure a complete interaction between the radicals and antioxidants. RSA was quantified by measuring the absorbance at 734 nm by using a UV−visible spectrophotometer. Ascorbic acid was used as the reference standard, and a blank ABTS solution was used as the control.[26] Radical scavenging activity was quantified using eq 1.

2.6.2. Assessment of the Ferric Reducing Antioxidant Power (FRAP) Activity. The FRAP assay was described by Benzie and Strain[27] with minor modifications, as per the experimental conditions, and the stock solutions were composed of 20 mM $FeCl_3{\cdot}6H_2O$, 10 mM TPTZ, and 300 mM acetate buffer at pH 3.[28] Freshly prepared FRAP working reagents were reacted with dispersed synthesized NPs and composites at different concentrations (20−100 μg/mL). The color intensity was measured by using a UV−visible spectrophotometer at 593 nm. Ascorbic acid was used as a standard antioxidant compound, and the optical densities of the samples were determined. All experimental analyses were performed in triplicate.

2.6.3. Assessment of Ferrous Ion Chelating Activity (FICA). In this study, we applied the modified protocol of Ebrahimzadeh et al.[29] to evaluate the ferrous ion chelation efficiency of the synthesized nanomaterials. The nanomaterial suspension (20−100 μg/mL with 2 mM $FeSO_4$ (50 μL), 5 mM ferrozine solution (100 μL), and distilled water (1850 μL) were combined. The reaction mixture was combined and left to stand for 10 min, after which the absorbance was measured at a 562 nm wavelength. Equation 1 was used to calculate the inhibition percentage (%) of the ferrozine-Fe^{2+} complex formation.

3. RESULTS AND DISCUSSION

3.1. Mechanism of Ag-Embedded ZnO Nanocomposite Formation via Thermal Decomposition. The mechanism of the synthesis of Ag-embedded ZnO nanocomposites via thermal decomposition can be understood through a series of physical and chemical transformations that occur during the mixing and annealing stages. Initially, $Zn(OH)_2$ and $AgNO_3$ are thoroughly mixed in varying weight ratios using a mortar and pestle to ensure uniform distribution of silver ions throughout the $Zn(OH)_2$. Mechanical grinding is essential for achieving a homogeneous mixture and ensuring uniform distribution of the silver precursor within $Zn(OH)_2$.[30] Thermal decomposition of $Zn(OH)_2$ occurred at 800 °C, producing ZnO NPs.

$$Zn(OH)_2 \xrightarrow{\Delta} ZnO + H_2O$$

Simultaneously, the Ag precursor, $AgNO_3$, also decomposes at high temperatures. This decomposition results in the formation of silver atoms along with the release of nitrogen dioxide and oxygen gas.[31]

$$2AgNO_3 \xrightarrow{\Delta} 2Ag + 2NO_2 + O_2$$

At this point, the silver ions (Ag^+) in $AgNO_3$ are reduced to silver atoms (Ag^0), which then aggregate to form Ag NPs. A high annealing temperature promotes the diffusion of Ag NPs on the ZnO surface.[32,33] The NPs nucleate and grow on the ZnO surface, embedding themselves owing to the high mobility of both Ag atoms and ZnO lattice structures at

https://doi.org/10.1021/acsomega.4c08896
ACS Omega 2025, 10, 11948−11960

elevated temperatures. The embedding was further facilitated by surface energy considerations, where Ag NPs were energetically driven to integrate with ZnO, thus stabilizing the composite. During the annealing process, a thermal decomposition reaction occurs, which allows the Ag NPs to become more intimately embedded in the ZnO crystal lattice. This resulted in the formation of a stable Ag-embedded ZnO nanocomposite with Ag NPs dispersed throughout the ZnO surface. The reaction between the ZnO surface and the Ag NPs may involve some degree of interaction or alloying at the interface, which enhances the stability and functional properties of the composite.

The overall result of this process was a series of Ag-embedded ZnO nanocomposites, labeled according to the weight percentage of Ag incorporated (1, 3, and 5%). The proposed overall reaction is summarized as follows:

$$Zn(OH)_2 + AgNO_3 \xrightarrow{\Delta} ZnONPs - AgNPs + NO_2 + H_2O + O_2$$

3.2. Optoelectronic Study. The optoelectronic properties of the synthesized ZnO NPs and Ag-embedded ZnO nanocomposites were investigated by analyzing their UV−vis diffuse reflectance spectroscopy (DRS) absorbance spectra (Figure 1a). The samples exhibited pronounced UV activity with intense absorption in the region between 250 and 365 nm. The absorption edge for ZnO NPs was identified at 375 nm, whereas the Ag-embedded ZnO nanocomposites showed a slightly blueshifted absorption edge near 369 nm, accompanied by varying absorption intensities. Notably, the ZnO-1 wt % Ag nanocomposite exhibited a higher absorption intensity compared to ZnO NPs, whereas the samples with higher Ag concentrations demonstrated a reduced absorption intensity. This reduction can be attributed to factors such as increased particle size, grain boundary effects, and changes in the grain size of ZnO.[34] The optical band gap (E_g) of the Ag-embedded ZnO nanocomposites was calculated using the Tauc equation (eq 2):

$$(\alpha h\nu)^2 = A(h\nu - E_g) \quad (2)$$

where A is the absorbance, h is Planck's constant, α is the absorption coefficient, ν is the photon frequency, and E_g is the band gap.

The optical band gap of ZnO NPs was determined to be 3.02 eV, which is lower than that 3.3 eV observed in bulk ZnO, owing to quantum confinement effects at the nanoscale.[35] However, for the Ag-embedded ZnO nanocomposites, the band gap was observed to increase in the range of 3.02−3.12 eV (as shown in Figure 1b) compared to ZnO NPs. The incorporation of Ag into the ZnO structure leads to additional electronic states below the conduction band (CB) of ZnO, which contributes to this band gap modification.[36] Interestingly, the band gap decreased with the incorporation of 3 wt % Ag compared to 1 wt % Ag, which can be explained by the Burstein−Moss effect.[37] The incorporation of Ag atoms introduces electron-localized states near the conduction band edge of ZnO, forming the lowest unoccupied molecular orbital (LUMO). This interaction leads to a change in the band gap, which enhances the optoelectronic properties of the nanocomposite.[38]

3.3. XRD Analysis. Figure 2 displays the XRD patterns of the ZnO NPs and Ag-embedded ZnO nanocomposites

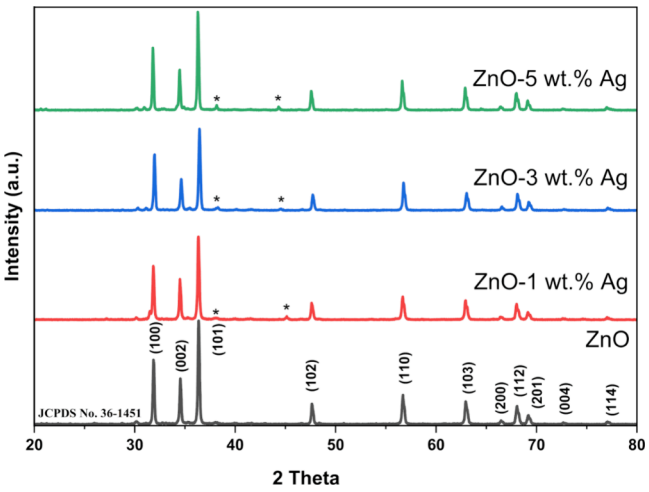

Figure 2. XRD diffraction patterns of ZnO NPs, ZnO-1 wt % Ag, ZnO-3 wt % Ag, and ZnO-5 wt % Ag nanocomposites.

recorded over a 2θ range of 20−80°. In the case of the ZnO NPs, prominent diffraction peaks were observed at approximately 2θ values of 31.8, 34.5, 36.3, 47.5, 56.5, 62.8, 66.3, 67.9, 69.1, 72.6, and 76.9°, corresponding to the (hkl) values of (100), (002), (101), (102), (110), (103), (200), (112), (201), (004), and (114), respectively, confirming the hexagonal wurtzite crystal structure (JCPDS no. 36-1451) of the pristine phase.[7,38] The XRD patterns of the Ag-ZnO nanocomposites (1, 3, and 5 wt %) display similar characteristic peaks to those of ZnO NPs, but with a slight decrease in peak intensities. This indicates that the overall hexagonal wurtzite structure of ZnO was maintained, despite the incorporation of Ag. Additionally, new diffraction peaks at approximately 2θ = 38.22 and 44.31°, corresponding to the (111) and (200) planes, respectively, were observed for the Ag-embedded ZnO nanocomposites, indicating the presence of Ag in the ZnO crystal lattice.[11] These patterns are consistent with JCPDS card no. 01-089-3722.[14]

For the ZnO-1 wt % Ag nanocomposite, an increase in the unit cell volume was observed, indicating lattice expansion due to the incorporation of Ag atoms into the ZnO crystal lattice. However, at high Ag concentrations (3 and 5 wt %), the unit cell volume decreased, suggesting a lattice contraction, likely due to the strain introduced by the Ag atoms. This shrinking effect can be attributed to the Ag atoms being interstitially located within the ZnO lattice at higher concentrations, whereas at 1 wt %, Ag atoms primarily substitute Zn atoms within the crystal structure. The Debye−Scherrer equation was employed to estimate the crystallite size of the ZnO NPs and Ag-ZnO nanocomposites.[14] As shown in Table S1, the crystallite size of the ZnO NPs was determined to be 46.88 nm, while the crystallite sizes of Ag-embedded ZnO nanocomposites varied between 45 and 50 nm, suggesting that the incorporation of Ag had a notable effect on the crystallite size.

3.4. Morphological Analysis. The SEM micrographs in Figure 3 show the morphologies of the ZnO NPs and Ag-embedded ZnO nanocomposites at various Ag concentrations. Figure 3a,b illustrates the ZnO NPs with a hexagonal rodlike structure, featuring lengths between 700 and 1500 nm and an average size of 1200 nm. These rodlike structures are characteristic of the ZnO wurtzite phase.[7] Upon the incorporation of 1 wt % Ag, as seen in Figure 3c,d, the surface morphology becomes more irregular, losing the sharp and

https://doi.org/10.1021/acsomega.4c08896
ACS Omega 2025, 10, 11948−11960

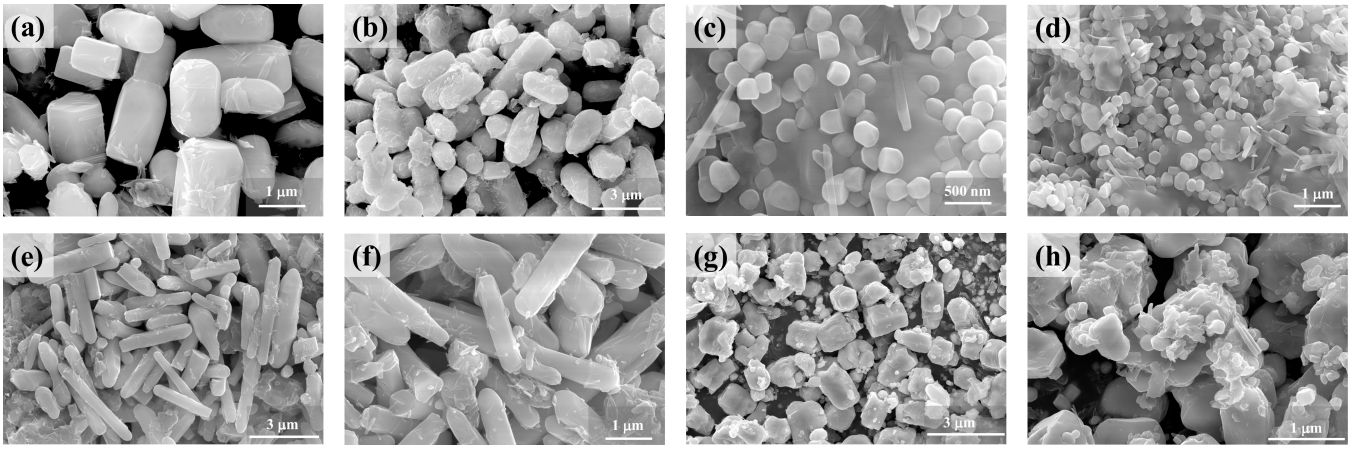

Figure 3. SEM micrographs of (a, b) ZnO NPs, (c, d) ZnO-1 wt % Ag, (e, f) ZnO-3 wt % Ag, and (g, h) ZnO-5 wt % Ag nanocomposites.

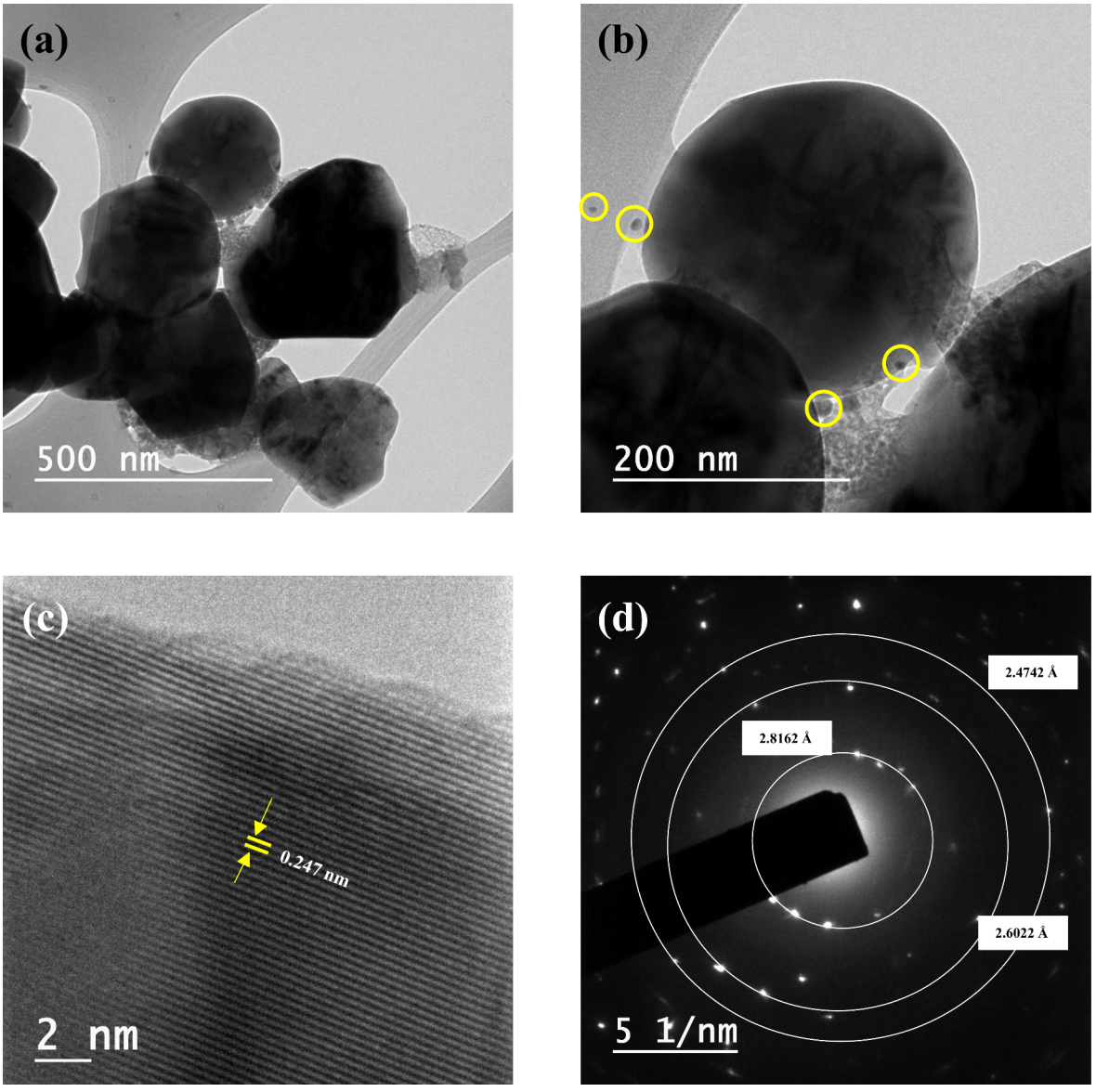

Figure 4. (a–c) TEM and HRTEM images of ZnO-5 wt % Ag nanocomposites with the loading of Ag pointed with a circular path. (d) SAED pattern of ZnO-5 wt % Ag nanocomposites.

defined hexagonal features of ZnO NPs. The particle sizes of the ZnO-1 wt % Ag nanocomposites range from 500 to 1000 nm, exhibiting smaller, polydispersed particles.[39] Figure 3e,f shows that ZnO-3 wt % Ag nanocomposites further show the

https://doi.org/10.1021/acsomega.4c08896
ACS Omega 2025, 10, 11948−11960

effect of Ag incorporation. The particles retained their structure, with sizes varying between 800 and 1600 nm and an average size of 1400 nm.[40] However, at a high Ag concentration (5 wt % Ag), as shown in Figure 3g,h, a reduction in particle size is observed, with the sizes ranging from 300 to 900 nm, and the average particle size is 700 nm.[41]

Figure 4 shows the surface morphology of ZnO-5 wt % Ag nanocomposites, which was characterized using TEM. The TEM images in Figure 4a,b reveal relatively spherical ZnO NPs with sizes ranging from 300 to 700 nm. Spherical Ag NPs, ~4 nm in size, were clearly visible on the surface of the ZnO NPs, as highlighted by the yellow circles in Figure 4b, confirming the formation of ZnO-Ag nanocomposites. The well-dispersed Ag NPs on the ZnO surface contributed to the enhanced photocatalytic and antioxidant activities of the composite, which may be due to the formation of additional active sites. High-resolution transmission electron microscopy (HRTEM) analysis (Figure 4c) reveals lattice fringes with a measured *d*-spacing of 0.247 nm, which corresponds to the (101) plane of the ZnO NPs. The HRTEM image shows the crystallinity of the ZnO-5 wt % Ag nanocomposites. The selected-area electron diffraction (SAED) pattern presented in Figure 4d confirms the polycrystalline nature of ZnO-5 wt % Ag nanocomposites, displaying diffraction rings that correspond to the (100), (002), and (101) *hkl* planes of ZnO, which aligns with the results obtained from X-ray diffraction patterns. The presence of distinct diffraction rings reinforces the structural integrity of the ZnO lattice after the Ag incorporation. The TEM and HRTEM images showed that Ag was integrated on the ZnO surface and the nanocomposites exhibited excellent crystallinity with well-dispersed Ag NPs on the ZnO surface. Elemental mapping of the ZnO-5 wt % Ag nanocomposites was further analyzed using TEM/EDS, as shown in Figure S1a–d. The presence of Ag is further supported by the Ag EDS image of the ZnO-5 wt % Ag nanocomposites, as shown in Figure S1d.

3.5. EDS Analysis. The EDS spectra in Figure S2 provide an elemental composition analysis of the Ag-embedded ZnO nanocomposites and ZnO NPs. In Figure S2a, the EDS spectrum of the ZnO NPs shows a composition of 78.7 wt % Zn and 21.3 wt % O, confirming the ZnO phase. This indicated the presence of a pristine ZnO structure before Ag incorporation. In Figure S2b, which corresponds to ZnO-1 wt % Ag, the EDS analysis shows 77.8 wt % Zn, 21.7 wt % O, and a trace amount of 0.5 wt % Ag. This confirms the introduction of a small amount of Ag into the ZnO. For ZnO-3 wt % Ag in Figure S2c, the EDS spectrum reveals 80.4 wt % Zn, 18.7 wt % O, and 0.9 wt % Ag, showing an increase in the Ag content while maintaining a stable ZnO structure. Figure S2d shows the EDS spectrum of ZnO-5 wt % Ag shows the highest silver incorporation with 2.3 wt % Ag, alongside 78.1 wt % Zn and 19.6 wt % O. This confirms the successful integration of a higher concentration of Ag into the ZnO nanocomposite. Increasing the Ag content across the samples (from 1 to 5 wt % Ag) is clearly reflected in the EDS spectra, confirming the gradual incorporation of Ag.

3.6. Raman Analysis. Figure 5 shows the Raman spectra of Ag-embedded ZnO nanocomposites and ZnO NPs. The prominent peak at ~437 cm^{-1} corresponds to the characteristic Raman-active optical phonon mode (E_2 high) of the hexagonal wurtzite structure of ZnO, which agrees with previously reported studies.[42,43] This peak is a signature of the structural integrity of the crystal and is highly sensitive to

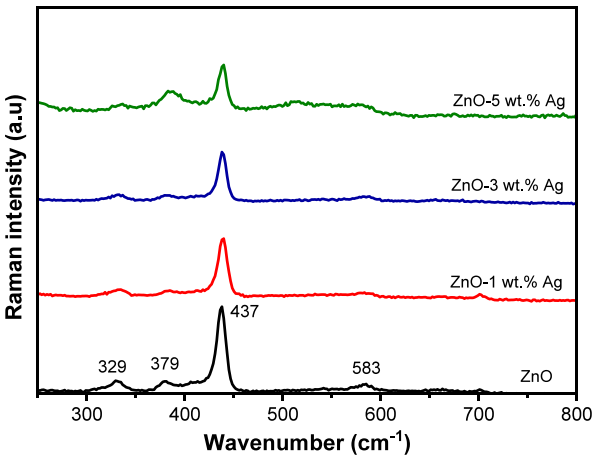

Figure 5. Raman spectra of ZnO NPs, ZnO-1 wt % Ag, ZnO-3 wt % Ag, and ZnO-5 wt % Ag nanocomposites.

modification. Additional peaks at 329 and 379 cm^{-1} are associated with second-order Raman modes, specifically the zone boundary phonon 3E2H−E2L and A_1 (TO) modes, respectively. The peak at 583 cm^1 is indicative of bulk ZnO and corresponds to the E_1 (LO) mode, which is often associated with oxygen vacancies or defects within the ZnO lattice. These Raman results are consistent with the findings of FTIR analysis, further validating the structural properties of the ZnO- and Ag-embedded ZnO nanocomposites. As the concentration of Ag increased, a reduction in the intensity of the 437 cm^{-1} band was observed. This decrease suggests the successful incorporation of Ag atoms into the ZnO crystal lattice, which disrupts the lattice vibrations associated with the E_2 high mode. The Ag-loaded ZnO nanocomposites affected the vibrational properties, as reflected by the diminished Raman peak intensity, signifying changes in the crystal structure due to Ag integration.

3.7. FTIR Analysis. Figure 6 shows the FTIR spectra of the Ag-embedded ZnO nanocomposites and ZnO NPs. Characteristic absorption bands were observed at 558 and 880 cm^{-1}, corresponding to Zn−O stretching vibrations, which are indicative of the wurtzite structure of ZnO.[7] These bands represent the fundamental vibrational modes of Zn−O bonds

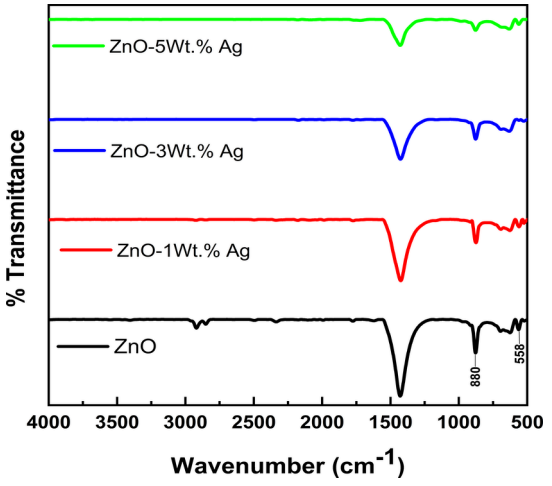

Figure 6. FTIR spectra of ZnO NPs, ZnO-1 wt % Ag, ZnO-3 wt % Ag, and ZnO-5 wt % Ag nanocomposites.

https://doi.org/10.1021/acsomega.4c08896
ACS Omega 2025, 10, 11948−11960

in the crystal lattice.[44] Upon the incorporation of Ag, the Ag-embedded ZnO nanocomposites showed a decrease in the intensity of the bands between 1300 and 1600 cm^{-1}, as well as a reduction in the intensity of the Zn−O bands at 558 and 880 cm^{-1}.[14,45,46] The gradual shift and reduction in the peak intensities support the hypothesis that Ag atoms are embedded in the ZnO crystal structure, influencing the bonding environment and the overall material properties.[46]

3.8. BET Analysis. Table 1 presents the BET analysis results, which indicate that the Ag-embedded ZnO nanocomposites possess relatively higher specific surface areas than the ZnO NPs. The ZnO NPs sample exhibited a specific surface area of 8.09 m^2/g, whereas the ZnO-5 wt % Ag nanocomposite had the highest surface area, with an S_{BET} value of 19.91 m^2/g. This increase in the surface area with a higher Ag content is attributed to enhanced particle dispersion and reduction in particle size, providing more active sites for catalytic reactions. The specific surface area values from BET analysis confirmed that increasing the Ag concentration in ZnO significantly enhanced the surface area, making Ag-embedded ZnO nanocomposites more effective for applications requiring a high surface area such as photocatalysis.

Table 1. Specific Surface Area Values of the Photocatalyst

sr. no.	photocatalyst	specific surface area (m^2/g)
1.	pristine ZnO	8.09
2.	ZnO-1 wt % Ag	15.46
3.	ZnO-3 wt % Ag	16.22
4.	ZnO-5 wt % Ag	19.91

3.9. Photocatalytic Activity. The photocatalytic degradation of the R6G dye under UV light was investigated using ZnO NPs and Ag-embedded ZnO nanocomposites as photocatalysts. The results showed an enhanced photocatalytic efficiency as the Ag concentration in ZnO increased. The absorbance spectra of R6G (Figure 7) demonstrated a gradual decrease in dye concentration over time, indicating progressive degradation (Table 2). While pristine ZnO NPs showed

Table 2. Photocatalytic Efficiency and Kinetic Study of Pristine ZnO and ZnO-Ag Nanocomposites

sr. no.	photocatalyst	photocatalytic degradation efficiency (%)	reaction rate constant (k) (min^{-1})	time required for degradation (min)
1.	pristine ZnO	60.99	2.27×10^{-3}	180
2.	ZnO-1 wt % Ag	69.80	2.89×10^{-3}	180
3.	ZnO-3 wt % Ag	85.32	4.63×10^{-3}	180
4.	ZnO-5 wt % Ag	93.36	6.54×10^{-3}	180

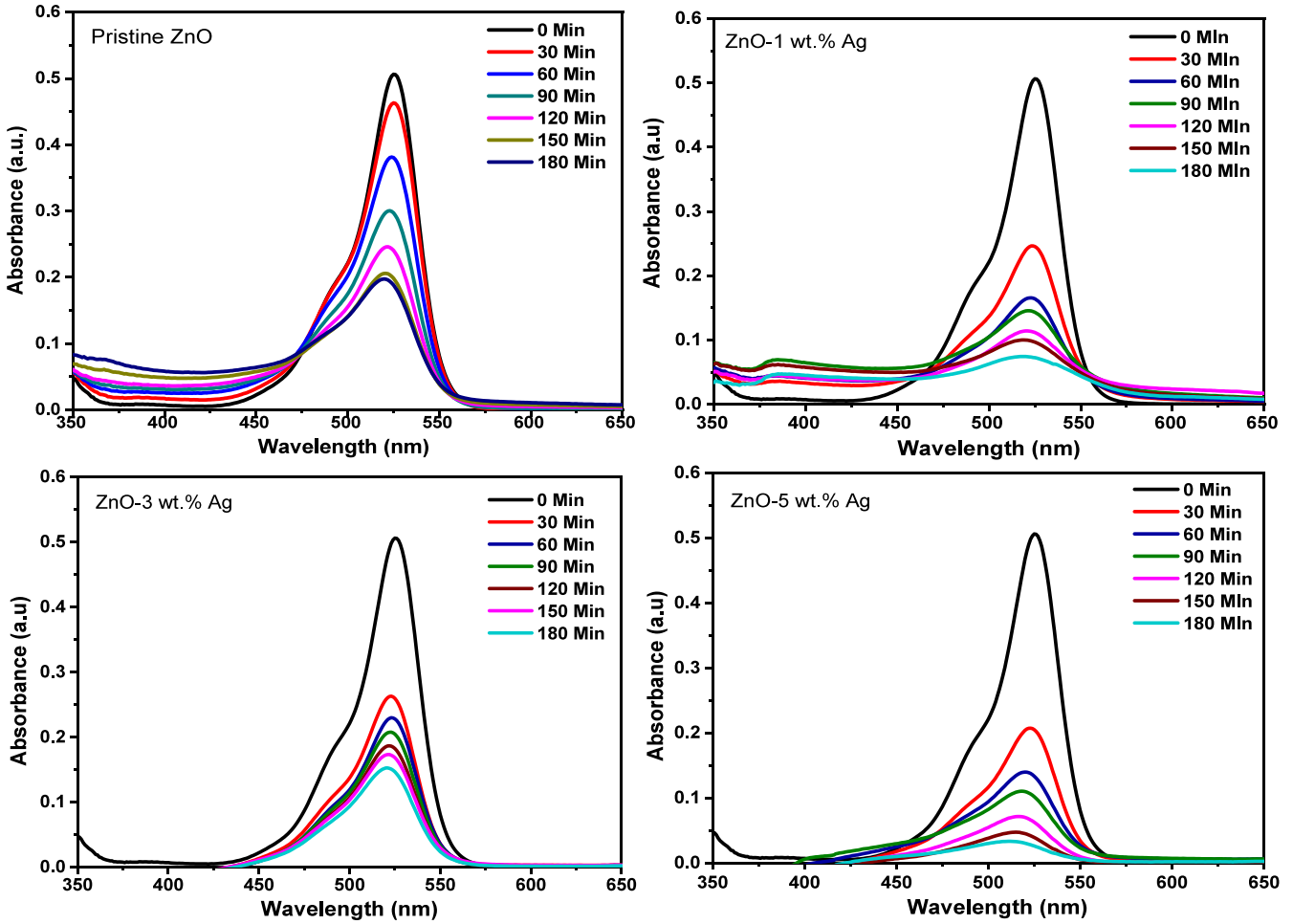

Figure 7. Absorbance spectra as a function of time for the photocatalytic degradation of the R6G dye in the presence of ZnO NPs, ZnO-1 wt % Ag, ZnO-3 wt % Ag, and ZnO-5 wt % Ag nanocomposites.

https://doi.org/10.1021/acsomega.4c08896
ACS Omega 2025, 10, 11948−11960

Table 3. Comparative Study of the Photocatalytic Degradation of Dyes Using Ag-ZnO Photocatalysts

sr. no.	photocatalyst	dye	concentration (mg/L)	photocatalyst amount (mg)	degradation time (min)	degradation efficiency (%)	rate constant (k) (min^{-1})	light source	reference
1.	Ag-ZnO nanocomposite	methylene blue (MB) and crystal violet (CV)	10	1 mg/mL	120 (MB) and 285 (CV)	91 (MB) and 83 (CV)	0.0127 (MB) and 0.0144 (CV)	sunlight	14
2.	Ag-ZnO composite	imidacloprid	20	20	60	80	N/A	UV light	50
3.	Ag@ZnO nanostructure	rhodamine B	10	1 mg/mL	90	99	0.03968	UV light	49
4.	Ag-ZnO nanoparticles	methylene blue/ rhodamine B/methyl orange	4	0.5 mg/mL	60	90	0.035	UV light	51
5.	Ag-embedded ZnO nanocomposite	R6G	10 mM	0.5 mg/mL	180	93.36	6.54×10^{-3}	mercury vapor UV lamp	this study

Scheme 1. Possible R6G Dye Degradation Mechanism in the Presence of the Ag-Embedded ZnO Nanocomposite Photocatalyst

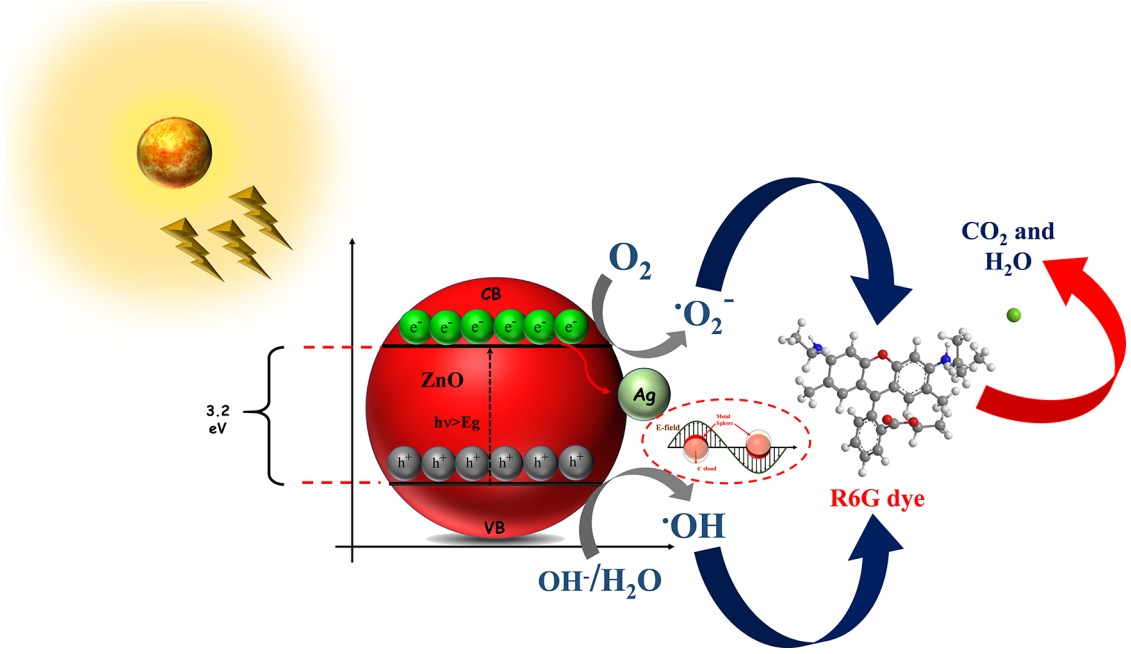

limited activity, resulting in 60.99% degradation after 180 min, the incorporation of Ag NPs enhances the degradation rate.[17,47] As the Ag content increased from 1 to 5 wt %, the photocatalytic efficiency was enhanced. ZnO-5 wt % Ag nanocomposites achieved a remarkable 93.36% degradation, accompanied by a significantly higher reaction rate constant (6.54×10^{-3} min^{-1}). This enhanced photocatalytic activity is attributed to the role of Ag NPs in promoting a more efficient charge separation and transfer. Ag NPs served as electron acceptors, accepting photogenerated electrons from the CB of ZnO. This facilitates a more effective electron transfer to surface-adsorbed oxygen species, forming ROS, which are superoxide radicals ($\bullet O_2^-$) that participate in the degradation of R6G.[48,49] The synergy between ZnO and Ag increases the availability of ROS and prolongs the lifetime of the charge carriers, thus suppressing electron−hole recombination. Consequently, the photocatalytic degradation of R6G is significantly accelerated. The enhanced surface area of the Ag-embedded ZnO nanocomposites further contributes to their high efficiency by providing more active sites for dye adsorption and subsequent degradation reactions. Table 3 presents a comparative analysis of the photocatalytic degradation of various dyes using different Ag-ZnO photocatalysts. The comparison covers key parameters such as the dye concentration, photocatalyst amount, degradation time, and degradation efficiency percentage.[49−51] These parameters are critical for evaluating the performance of different Ag-ZnO photocatalysts in dye degradation under various conditions.

3.8.1. Mechanism of Photocatalytic Degradation. The mechanism for the photocatalytic degradation of R6G using Ag-embedded ZnO nanocomposites is shown in Scheme 1. UV light irradiation with photons with energies greater than the band gap of ZnO (3.2 eV) induces the excitation of electrons from the valence band (VB) to the conduction band (CB), resulting in the formation of electron−hole pairs.[10,14] This process can be expressed as follows:

$$\mathrm{ZnO} + h\nu\ (\mathrm{UV\ light}) \rightarrow e^-_{CB} + h^+_{VB}$$

However, the rapid recombination of these electron−hole pairs often limits the efficiency of the photocatalytic reaction.[47] To address this issue, AgNPs were embedded in ZnO, which significantly reduced the level of recombination. This reduction is largely due to the LSPR effect of AgNPs, which enhances visible-light absorption and promotes the separation of charge carriers.[33,47] The LSPR effect occurs when the conduction band electrons in Ag nanoparticles resonate with

https://doi.org/10.1021/acsomega.4c08896
ACS Omega 2025, 10, 11948−11960

the incident light, particularly in the visible region, extending the absorption capabilities of the photocatalyst.[49] The AgNPs act as electron acceptors, capturing electrons from the CB of ZnO, as shown in Scheme 1.

$$e^-_{CB(ZnO)} \rightarrow e^-_{Ag}$$

Without this electron transfer, electron−hole recombination would occur, diminishing the photocatalytic efficiency. The captured electrons in the AgNPs interact with oxygen molecules adsorbed on the surface of the photocatalyst, generating superoxide radicals ($\bullet O_2^-$).[15]

$$e^-_{Ag} + O_2 \rightarrow \bullet O_2^-$$

These superoxide radicals are highly reactive and can subsequently interact with water molecules to generate hydroxyl radicals (•OH), which act as oxidizing agents.[14]

$$\bullet O_2^- + H_2O \rightarrow \bullet OH + OH^-$$

Simultaneously, the photogenerated holes (h^+) in the VB of ZnO oxidize water molecules to produce additional hydroxyl radicals.

$$h^+_{VB(ZnO)} + H_2O \rightarrow \bullet OH + H^+$$

Both superoxide ($\bullet O_2^-$) and hydroxyl radicals (•OH) were the primary ROS responsible for the degradation of R6G. These ROS attack the dye molecules, initiating a series of oxidative reactions that break down R6G into smaller and less harmful compounds, including CO_2 and H_2O.

$$R6G + \bullet OH \rightarrow CO_2 + H_2O + \text{degradation products}$$

The photocatalytic efficiency was significantly enhanced owing to the synergy between ZnO and the AgNPs in the ZnO-5 wt % Ag nanocomposite, particularly driven by the LSPR effect of AgNPs, which extends the absorption range into the visible-light spectrum. This effect aids in the excitation of electrons and facilitates the efficient generation of ROS, thereby improving the degradation process.[47]

3.10. Recyclability Study. Recyclability is a key factor in designing cost-effective and sustainable photocatalysts that must exhibit a high adsorption capacity and efficient desorption to allow for repeated use without a significant loss of activity, ultimately minimizing operational costs. In this study, the synthesized nanocomposites were subjected to a recyclability assessment using a centrifuge to recover the materials after each photocatalytic reaction cycle. This method ensured the effective separation and reuse of the nanocomposites. As shown in Figure 8, the ZnO-5 wt % Ag nanocomposite maintained a removal efficiency of >91% for the R6G dye even after five consecutive cycles. This demonstrates the recyclability and sustainability of the ZnO-5 wt % Ag nanocomposite as a photocatalyst in the degradation of the R6G dye. The as-synthesized ZnO-5 wt % Ag nanocomposite exhibited excellent recyclability, retaining its effectiveness in removing dyes across multiple cycles, thereby affirming its potential for practical applications in wastewater treatment. Figure S3 presents the cycle removal rate for the ZnO-3 wt % Ag nanocomposite over five photocatalytic cycles, which is provided in the Supporting Information. The stability of the photocatalyst was further confirmed by XRD and FTIR analyses, which showed no significant structural changes in the ZnO-5 wt % Ag nanocomposite after five consecutive photocatalytic cycles

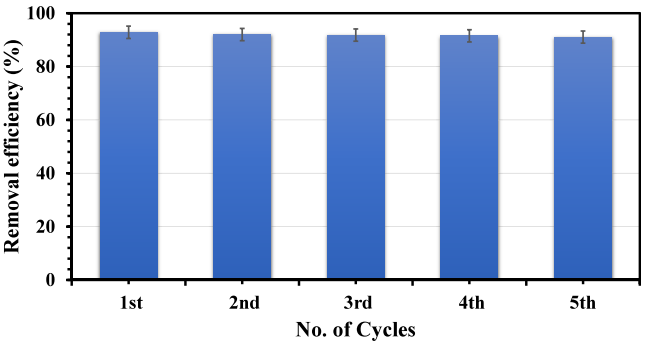

Figure 8. Recyclability study of the ZnO-5 wt % Ag nanocomposite for the degradation of the R6G dye over five cycles.

(Figures S4 and S5). This indicates the robust stability of the photocatalyst, suggesting its suitability for long-term applications without a significant loss of efficiency.

3.11. Antioxidant Study. Antioxidants have garnered significant interest in medical research because of their potent ability to inhibit ROS-induced pathogenesis, which is a critical factor in the development of various degenerative diseases including cancer and cardiovascular conditions.[52] Nanomaterials with different morphologies, including nanoparticles,[2] nanorods,[7] and nanocomposites,[44] have demonstrated substantial *in vitro* biological activities, including antioxidant effects.[52−54] The findings of this study suggest that ZnO NPs and their composites with Ag NPs have significant potential for biomedical engineering applications (Figure 9).

The DPPH assay evaluates the free radical scavenging ability of nanomaterials with antioxidant properties by monitoring the reduction of the stable DPPH radical, which has a deep purple color. The nanomaterials donate electrons to the DPPH radical, neutralizing it and causing a color change from purple to yellow, which is measurable by a decrease in absorbance at 517 nm.[55,56] The greater the reduction in absorbance, the higher the free radical scavenging activity and thus the stronger the antioxidant potential of the material.[57] At a concentration of 100 μg/mL, the DPPH radical scavenging activities of the ZnO NPs, ZnO-1 wt % Ag, ZnO-3 wt % Ag, and ZnO-5 wt % Ag nanocomposites were 29.56 ± 0.39, 25.42 ± 1.22, 27.19 ± 1.04, and 32.52 ± 1.19%, respectively (Figure 9a). Among the tested samples, ZnO-5 wt % Ag nanocomposites exhibited the highest DPPH scavenging activity, demonstrating superior free radical neutralization capacity.

The ABTS assay offers an alternative method for evaluating the antioxidant capacity of nanomaterials. The assay involves the generation of the ABTS•+ chromophore, which has a characteristic blue/green color, via the reaction of ABTS with potassium persulfate.[2] Antioxidants reduce the chromophore, resulting in a decrease in the color intensity, which can be quantified using UV−vis spectroscopy. At a concentration of 100 μg/mL, the ABTS radical scavenging activities of the ZnO NPs, ZnO-1 wt % Ag, ZnO-3 wt % Ag, and ZnO-5 wt % Ag were 81.83 ± 1.16, 85.92 ± 1.48, 90.01 ± 2.11, and 92.47 ± 2.28%, respectively (Figure 9b). These results demonstrate that ZnO-5 wt % Ag nanocomposites exhibit the highest ABTS scavenging activity, indicating their superior antioxidant potential. The antioxidant capacity of the synthesized nanomaterials increased significantly at higher concentrations (20, 40, 60, 80, and 100 μg/mL), suggesting concentration-dependent activity.

https://doi.org/10.1021/acsomega.4c08896
ACS Omega 2025, 10, 11948−11960

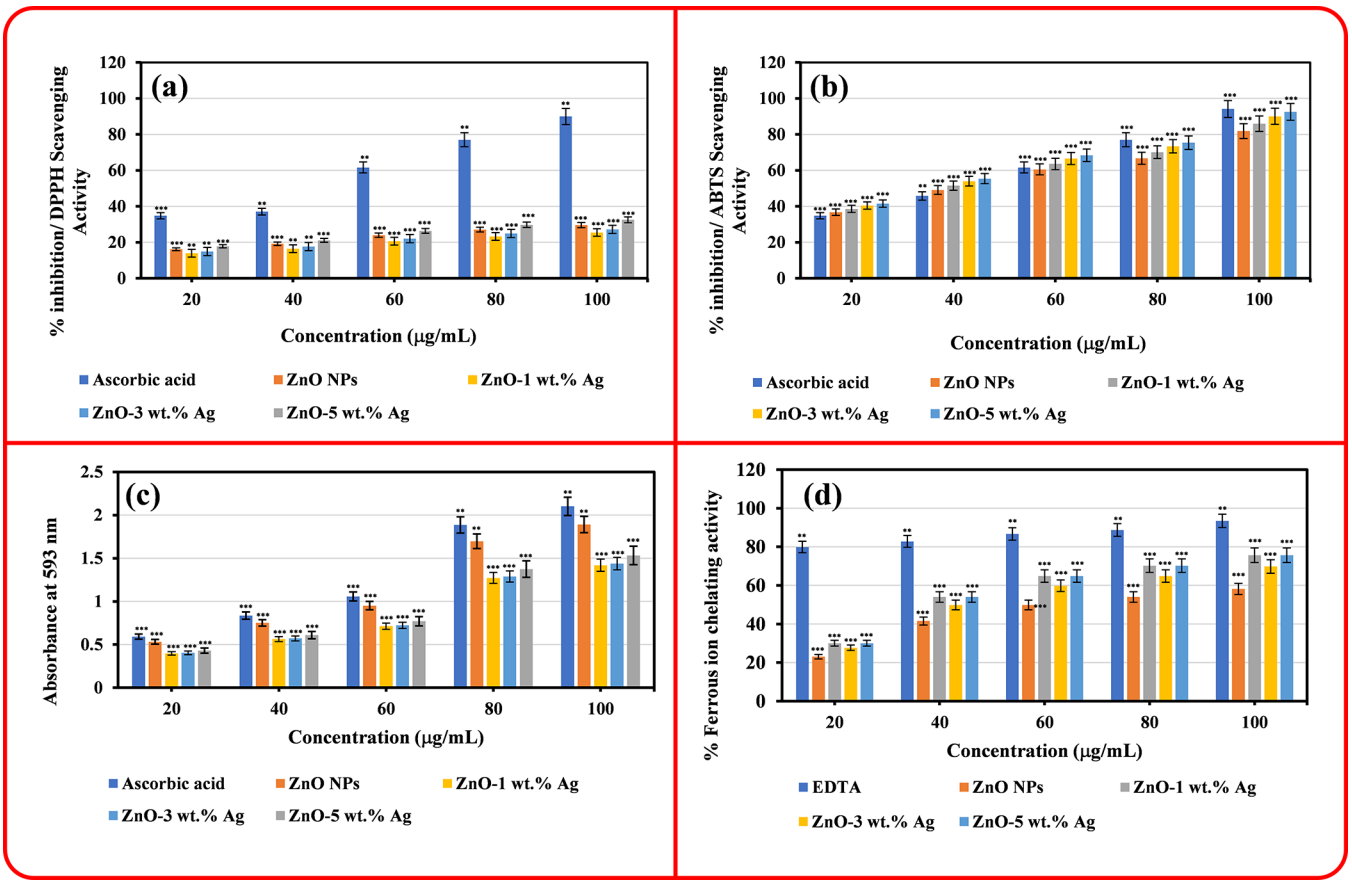

Figure 9. Antioxidant activities of ZnO NPs, ZnO-1 wt % Ag, ZnO-3 wt % Ag, and ZnO-5 wt % Ag nanocomposites evaluated through (a) DPPH radical scavenging activity, (b) ABTS radical scavenging activity, (c) FRAP activity, and (d) FIC activity. The data shown is statistically significant, with $*P < 0.01$, $**P < 0.001$, and $***P < 0.0001$.

The FRAP assay measures the antioxidant capacity of nanomaterials by assessing their ability to reduce Fe^{3+} to Fe^{2+}. The increase in absorbance at 593 nm is correlated with higher reducing power.[46] In this study, the FRAP activity of the synthesized nanomaterials was evaluated at concentrations ranging from 20 to 100 μg/mL, with measurements taken at 593 nm. The highest FRAP activities were observed for ZnO NPs (1.89 ± 0.17 O.D.), ZnO-1 wt % Ag (1.41 ± 0.11 O.D.), ZnO-3 wt % Ag (1.43 ± 0.13 O.D.), and ZnO-5 wt % Ag (1.53 ± 0.03 O.D.) (Figure 9c). ZnO NPs exhibited the strongest FRAP activity, followed closely by ZnO-5 wt % Ag nanocomposites, underscoring their potential for reducing ferric ions.[54]

The FIC activity of nanomaterials is crucial for preventing the formation of harmful free radicals by chelating Fe^{2+} ions, thereby inhibiting their participation in Fenton-type reactions, which can induce oxidative stress and lead to cellular damage.[58,59] Owing to their high surface area and reactivity, nanomaterials are highly effective at binding ferrous ions, making them valuable for biomedical applications aimed at mitigating oxidative stress.[60,61] At a concentration of 100 μg/mL, the FIC activities of the ZnO NPs, ZnO-1 wt % Ag, ZnO-3 wt % Ag, and ZnO-5 wt % Ag nanocomposites were 58.17 ± 2.04, 63.41 ± 1.05, 69.81 ± 1.22, and 75.63 ± 0.81%, respectively (Figure 9d). The ZnO-5 wt % Ag nanocomposites demonstrated the highest FIC activity, highlighting their strong potential to chelate ferrous ions and reduce oxidative stress.

4. CONCLUSIONS

In this study, Ag-embedded ZnO nanocomposites with varying Ag concentrations (1, 3, and 5 wt %) were successfully synthesized using a sol−gel method followed by thermal decomposition. The ZnO-5 wt % Ag nanocomposite exhibited the highest photocatalytic efficiency, achieving 93.36% degradation of the rhodamine 6G (R6G) dye under UV irradiation with a reaction rate constant of 6.54×10^{-3} min^{-1}. This performance is significantly enhanced to that of pristine ZnO (8.09 m^2/g) and ZnO-1 wt % Ag (14.88 m^2/g), with the ZnO-5 wt % Ag nanocomposite demonstrating the highest specific surface area of 19.91 m^2/g, as measured by BET analysis. The recyclability of the nanocomposite, retaining over 91% of its initial photocatalytic activity after five cycles, indicates its potential for sustainable long-term use in practical applications. In antioxidant activity, the ZnO-5 wt % Ag nanocomposite showed exceptional free radical scavenging capacity, with a DPPH RSA of 87.12%, an ABTS RSA of 90.45%, and an FIC inhibition of 80.25%, highlighting its strong antioxidant potential. These values are significantly higher than those of the other nanocomposites and pristine ZnO, confirming its effectiveness in mitigating oxidative stress. These findings underscore the dual functionality of Ag-embedded ZnO nanocomposites in both photocatalytic and antioxidant applications, making them promising candidates for environmental remediation and biomedical applications. Future research will focus on further exploring their scalability, visible-light photocatalytic performance, and industrial-scale

https://doi.org/10.1021/acsomega.4c08896
ACS Omega 2025, 10, 11948−11960

applications, particularly in wastewater treatment and healthcare.

■ ASSOCIATED CONTENT

Data Availability Statement

The data underlying this study are available in the published article and its Supporting Information.

Supporting Information

The Supporting Information is available free of charge at https://pubs.acs.org/doi/10.1021/acsomega.4c08896.

Schematic representation of the synthesis of Ag-embedded ZnO nanocomposites (Scheme S1); structural parameters of Ag-embedded ZnO nanocomposites (Table S1); elemental mapping of Ag-embedded ZnO nanocomposites (Figure S1); EDS spectra of Ag-embedded ZnO nanocomposites (Figure S2); recyclability study of the ZnO-3 wt % Ag nanocomposite for the degradation of the R6G dye (Figure S3); XRD spectra of 5 wt % Ag-ZnO nanocomposites after photocatalytic degradation of the R6G dye over five cycles (Figure S4); XRD spectra of 5 wt % Ag-ZnO nanocomposites after photocatalytic degradation of the R6G dye over five cycles (Figure S5) (PDF)

■ AUTHOR INFORMATION

Corresponding Author

Avinash A. Ramteke − *Department of Chemistry, Devchand College, Arjunnagar, Kolhapur, MH 591237, India;* orcid.org/0000-0002-8544-9223; Email: dravinash03@gmail.com

Authors

Sachin K. Dhawale − *Department of Applied Sciences & Humanities, Gharda Institute of Technology, Ratnagiri, MH 415708, India*

Prashant D. Sarvalkar − *School of Nanoscience and Biotechnology, Shivaji University, Kolhapur, MH 416004, India;* orcid.org/0000-0001-6768-6797

Chetan S. Shinde − *Department of Applied Sciences & Humanities, Gharda Institute of Technology, Ratnagiri, MH 415708, India*

Neeraj R. Prasad − *School of Nanoscience and Biotechnology, Shivaji University, Kolhapur, MH 416004, India*

Kalyanrao M. Garadkar − *Department of Chemistry, Shivaji University, Kolhapur, MH 416004, India;* orcid.org/0000-0002-5733-9895

Kiran Kumar K. Sharma − *Department of Applied Sciences & Humanities, Gharda Institute of Technology, Ratnagiri, MH 415708, India;* orcid.org/0000-0003-1823-1934

Complete contact information is available at: https://pubs.acs.org/10.1021/acsomega.4c08896

Notes

The authors declare no competing financial interest.

■ ACKNOWLEDGMENTS

We are thankful to the Department of Chemistry, Devchand College, Arjunnagar, and School of Nanoscience and Biotechnology, Shivaji University Kolhapur, (M.S.) India, for providing the necessary laboratory facilities to study the applications of the synthesized materials.

■ REFERENCES

(1) Prasad, R. D.; Prasad, N. R.; Prasad, R. B.; Prasad, R. Y.; Prasad, S. R.; Gour, M.; et al. A Critical Review on Bio-mimetic Synthesis of Transition Metal Nanoparticles: Their Biomedical Applications in Veterinary Medicine. *ES Food Agrofor* **2023**.

(2) Sarvalkar, P. D.; Jamadar, A. S.; kakade, S. S.; Magdum, A. B.; Pawar, P. K.; Yadav, J. B.; et al. Biogenic synthesis of Co3O4 nanoparticles from Aloe barbadensis extract: Antioxidant and antimicrobial activities, and photocatalytic degradation of azo dyes. *Results Eng.* **2024**, *22*, No. 102094.

(3) Prasad, R. D.; Sarvalkar, P. D.; Prasad, N.; Prasad, R. S.; Prasad, R. B.; Prasad, R. R.; et al. Emerging Trends of Bioactive Nanomaterials in Modern Veterinary Science and Animal Husbandry. *ES Food Agrofor* **2024**, 1−89.

(4) Prasad, R. D.; Desai, C. B.; Srivastava, O. P.; Prasad, S. R.; Bhat, T. S.; Kamble, B.; et al. A Critical Review on Recent Developments in Advanced Supercapacitors for Veterinary Medicine. *ES Food Agrofor.* **2023**, *11*, 805.

(5) Prasad, R. D.; Charmode, N.; Shrivastav, O. P.; Prasad, S. R.; Moghe, A.; Samant, A.; et al. A Review on Concept of Nanotechnology in Veterinary Medicine. *ES Food Agrofor* **2021**, 28−60.

(6) Yu, W.; Zhang, J.; Peng, T. New insight into the enhanced photocatalytic activity of N-, C- and S-doped ZnO photocatalysts. *Appl. Catal., B* **2016**, *181*, 220−227.

(7) Sarvalkar, P. D.; Kamble, S. S.; Powar, P. S.; Kakade, S. S.; Jamadar, A. S.; Thounaojam, P.; et al. Synthesized rGO/f-MWCNT-architectured 1-D ZnO nanocomposites for azo dyes adsorption, photocatalytic degradation, and biological applications. *Catal. Commun.* **2024**, *187*, No. 106846.

(8) Ramola, R. C.; Negi, S.; Rawat, M.; Singh, R. C.; Singh, F. Annealing Effects on Gas Sensing Response of Ga-Doped ZnO Thin Films. *ACS Omega* **2021**, *6*, 11660−11668.

(9) Manohar, A.; Park, J.; Geleta, D. D.; Krishnamoorthi, C.; Thangam, R.; Kang, H.; et al. Synthesis and characterization of ZnO nanoparticles for photocatalysis, antibacterial and cytotoxicity in kidney cancer (A498) cell lines. *J. Alloys Compd.* **2021**, *874*, No. 159868.

(10) Weldegebrieal, G. K. Synthesis method, antibacterial and photocatalytic activity of ZnO nanoparticles for azo dyes in wastewater treatment: A review. *Inorg. Chem. Commun.* **2020**, *120*, No. 108140.

(11) Pimpliskar, P. V.; Motekar, S. C.; Umarji, G. G.; Lee, W.; Arbuj, S. S. Synthesis of silver-loaded ZnO nanorods and their enhanced photocatalytic activity and photoconductivity study. *Photochem. Photobiol. Sci.* **2019**, *18*, 1503−1511.

(12) Zhang, Y.; Gao, X.; Zhi, L.; Liu, X.; Jiang, W.; Sun, Y.; et al. The synergetic antibacterial activity of Ag islands on ZnO (Ag/ZnO) heterostructure nanoparticles and its mode of action. *J. Inorg. Biochem* **2014**, *130*, 74−83.

(13) Visnapuu, M.; Rosenberg, M.; Truska, E.; Nõmmiste, E.; Šutka, A.; Kahru, A.; et al. UVA-induced antimicrobial activity of ZnO/Ag nanocomposite covered surfaces. *Colloids Surfaces B Biointerfaces* **2018**, *169*, 222−232.

(14) Karvekar, O. S.; Sarvalkar, P. D.; Vadanagekar, A. S.; Singhan, R. D.; Jadhav, S. M.; Nimbalkar, M. S.; et al. Biogenic synthesis of silver anchored ZnO nanorods as nano catalyst for organic transformation reactions and dye degradation. *Appl. Nanosci* **2022**, *12*, 2207−2226.

(15) Andrade, G. R. S.; Nascimento, C. C.; Lima, Z. M.; Teixeira-Neto, E.; Costa, L. P.; Gimenez, I. F. Star-shaped ZnO/Ag hybrid nanostructures for enhanced photocatalysis and antibacterial activity. *Appl. Surf. Sci.* **2017**, *399*, 573−582.

(16) Adhavan, R.; Selvam, K.; Prakash, P.; Kirubakaran, D.; Shivakumar, M. S. Larvicidal, bactericidal, antioxidant, hypoglycemic effects and anti-proliferative activity of phyto-synthesized Ag-ZnO nanocomposites using Eranthemum roseum (Vahl) R.Br. leaf extract against Aedes aegypti and Culex quinquefasciatus mosquito vectors. *J. Nat. Pestic Res.* **2024**, *10*, No. 100093.

(17) Tran, M. L.; Nguyen, C. H.; Fu, C. C.; Juang, R. S. Hybridizing Ag-Doped ZnO nanoparticles with graphite as potential photocatalysts for enhanced removal of metronidazole antibiotic from water. *J. Environ. Manage* **2019**, *252*, No. 109611.
(18) Pirhashemi, M.; Habibi-Yangjeh, A. Ultrasonic-assisted preparation of plasmonic ZnO/Ag/Ag2WO4 nanocomposites with high visible-light photocatalytic performance for degradation of organic pollutants. *J. Colloid Interface Sci.* **2017**, *491*, 216−229.
(19) Loka, C.; Lee, K. S. Enhanced Visible-Light-Driven Photocatalysis of Ag/Ag2O/ZnO Nanocomposite Heterostructures. *Nanomaterials* **2022**, *12*, 2528.
(20) Zhang, Q.; Li, J.; Xu, M. Nanocomposites for Visible Light-Driven Photocatalytic Degradation: Basic understanding and outlook. *J. Phys. D Appl. Physics* **2022**, *55*, No. 483001.
(21) Chang, X.; Li, Z.; Zhai, X.; Sun, S.; Gu, D.; Dong, L.; et al. Efficient synthesis of sunlight-driven ZnO-based heterogeneous photocatalysts. *Mater. Des* **2016**, *98*, 324−332.
(22) Padvi, M. N.; Hiremath, N. G.; Prasad, S. R.; Nayak, A. K.; Bohara, R. A.; Attrar, Y.; et al. Bos taurus Urine Assisted Biosynthesis of CuO Nanomaterials: A New Paradigm of Antimicrobial and Antineoplatic Therapy. *Macromol. Symp.* **2020**, *392*, No. 1900172.
(23) Alwan, R. M.; Kadhim, Q. A.; Sahan, K. M.; Ali, R. A.; Mahdi, R. J.; Kassim, N. A.; et al. Synthesis of Zinc Oxide Nanoparticles via Sol − Gel Route and Their Characterization. *Nanosci. Nanotechnol.* **2015**, *5*, 1−6.
(24) Suryawanshi, S.; Kshirsagar, P.; Kamble, P.; Bapat, V.; Jadhav, J. Systematic enhancement of l-DOPA and secondary metabolites from Mucuna imbricata: Implication of precursors and elicitors in Callus culture. *South African Journal of Botany* **2022**, *144*, 419−429.
(25) Brand-Williams, W.; Cuvelier, M. E.; Berset, C. Use of a Free Radical Method to Evaluate Antioxidant Activity. *LWT Food Sci. Technol.* **1995**, *28*, 25−30.
(26) Padvi, M. N.; Prasad, S. R.; Shaikh, Y. I.; Suryawanshi, S. S.; Samant, A. P.; Chaudhary, L. S.; et al. Bio - inspired synthesis of catalytically and biologically active palladium nanoparticles using Bos taurus urine. *SN Appl. Sci.* **2020**, *2*, 1−12.
(27) Benzie, I. F. F.; Strain, J. J. The ferric reducing ability of plasma (FRAP) as a measure of "antioxidant power": The FRAP assay. *Anal. Biochem.* **1996**, *239*, 70−76.
(28) Thamke, V.; Suryawanshi, S.; Aware, C.; Shinde, B.; Patil, D.; Rane, M.; Chaudahari, A.; Tapase, S.; Jadhav, J. Mucuna laticifera: unprecedented L - dopa content and its role in neurodegenerative and inflammatory conditions. *3 Biotech* **2024**, 126.
(29) Ebrahimzadeh, M. A.; Pourmorad, F.; Bekhradnia, A. R. Iron chelating activity, phenol and flavonoid content of some medicinal plants from Iran. *Afr. J. Biotechnol.* **2008**, *7*, 3188−3192.
(30) Gupta, J.; Mohapatra, J.; Bahadur, D. Visible light driven mesoporous Ag-embedded ZnO nanocomposites: reactive oxygen species enhanced photocatalysis, bacterial inhibition and photodynamic therapy. *Dalt Trans* **2017**, *46*, 685−696.
(31) Sharma, P.; Lotey, G. S.; Singh, S.; Verma, N. K. Solution-combustion: The versatile route to synthesize silver nanoparticles. *J. Nanoparticle Res.* **2011**, *13*, 2553−2561.
(32) Sun, F.; Qiao, X.; Tan, F.; Wang, W.; Qiu, X. One-step microwave synthesis of Ag/ZnO nanocomposites with enhanced photocatalytic performance. *J. Mater. Sci.* **2012**, *47*, 7262−7268.
(33) Mohammadzadeh, S.; Olya, M. E.; Arabi, A. M.; Shariati, A.; Khosravi Nikou, M. R. Synthesis, characterization and application of ZnO-Ag as a nanophotocatalyst for organic compounds degradation, mechanism and economic study. *J. Environ. Sci. (China)* **2015**, *35*, 194−207.
(34) Tazerout, M.; Chelouche, A.; Touam, T.; Djouadi, D.; Boudjouan, F.; Khodja, S.; et al. Effects of sol concentration on structural, morphological and optical waveguiding properties of sol-gel ZnO nanostructured thin films. *Eur. Phys. J.: Appl. Phys.* **2014**, *67*, 10502.
(35) Tarwal, N. L.; Patil, P. S. Enhanced photoelectrochemical performance of Ag-ZnO thin films synthesized by spray pyrolysis technique. *Electrochim. Acta* **2011**, *56*, 6510−6516.
(36) Xue, H.; Xu, X. L.; Chen, Y.; Zhang, G. H.; Ma, S. Y. Influence of Ag-doping on the optical properties of ZnO films. *Appl. Surf. Sci.* **2008**, *255*, 1806−1810.
(37) Donia, D.; Litaiem, Y.; Karyaoui, M.; Radhouane, C. Correlation between photoelectrochemical and photoluminescence measurements of Ag-doped ZnO/ITO. *Eur. Phys. J.: Appl. Phys.* **2021**, 20401.
(38) Jawale, V.; Gugale, G.; Chaskar, M.; Pandit, S.; Pawar, R.; Suryawanshi, S.; et al. Two- and three-dimensional zinc oxide nanostructures and its photocatalytic dye degradation performance study. *J. Mater. Res.* **2021**, *36*, 1573−1583.
(39) Hosseini, S. M.; Sarsari, I. A.; Kameli, P.; Salamati, H. Effect of Ag doping on structural, optical, and photocatalytic properties of ZnO nanoparticles. *J. Alloys Compd.* **2015**, *640*, 408−15.
(40) Taabouche, A.; Bouabellou, A.; Kermiche, F.; Hanini, F.; Sedrati, C.; Bouachiba, Y.; et al. Preparation and characterization of Al-doped ZnO piezoelectric thin films grown by pulsed laser deposition. *Ceram. Int.* **2016**, *42*, 6701−6.
(41) Kayani, Z. N.; Saleemi, F.; Batool, I. Effect of calcination temperature on the properties of ZnO nanoparticles. *Appl. Phys. A Mater. Sci. Process* **2015**, *119*, 713−20.
(42) Satpal, S. B.; Athawale, A. A. Insights into the effect of halide enriched ZnO synthesized using tetrabutylammonium halides toward photocatalytic degradation of Rhodamine 6G. *Environ. Prog. Sustain Energy* **2021**, *40*, 40.
(43) Satpal, S. B.; Athawale, A. A. Synthesis of ZnO and Nd doped ZnO polyscales for removal of rhodamine 6G dye under UV light irradiation. *Mater. Res. Express* **2018**, *5*, No. 085501.
(44) Karvekar, O. S.; Vadanagekar, A. S.; Sarvalkar, P. D.; Suryawanshi, S. S.; Jadhav, S. M.; Singhan, R. D.; et al. *Bos taurus* (A - 2) urine assisted bioactive cobalt oxide anchored ZnO: a novel nanoscale approach. *Sci. Rep* **2022**, *12*, 15584.
(45) Sarvalkar, P. D.; Mandavkar, R. R.; Nimbalkar, M. S.; Sharma, K. K.; Patil, P. S.; Kamble, G. S.; et al. Bio-mimetic synthesis of catalytically active nano-silver using Bos taurus (A-2) urine. *Sci. Rep* **2021**, *11*, 16934.
(46) Kumbhar, G. S.; Patil, S. V.; Sarvalkar, P. D.; Vadanagekar, A. S.; Karvekar, O. S.; Patil, S. S.; et al. Synthesis of a Ag/rGO nanocomposite using *Bos taurus indicus* urine for nitroarene reduction and biological activity. *RSC Adv.* **2022**, *12*, 35598−612.
(47) Sayed, M.; Yu, J.; Liu, G.; Jaroniec, M. Non-noble plasmonic metal-based photocatalysts. *Chem. Rev.* **2022**, *122*, 10484−10537.
(48) Jawale, V.; Al-fahdawi, A.; Salve, S.; Pandit, S.; Dawange, G.; Gugale, G.; et al. 6, 13-pentacenequinone/zinc oxide nanocomposites for organic dye degradation. *Mater. Today Proc.* **2022**, *52*, 17−20.
(49) Sun, Y.; Zhao, Z.; Li, G.; Li, P.; Zhang, W.; Han, Z.; et al. Synthesis and characterization of Ag@ZnO nanostructures for photocatalytic degradation of rhodamine B: influence of calcination temperature and Ag content. *Appl. Phys. A Mater. Sci. Process* **2017**, *123*, 1−9.
(50) Kanwal, M.; Tariq, S. R.; Chotana, G. A. Photocatalytic degradation of imidacloprid by Ag-ZnO composite. *Environ. Sci. Pollut Res.* **2018**, *25*, 27307−20.
(51) Liu, Y.; Zhang, Q.; Xu, M.; Yuan, H.; Chen, Y.; Zhang, J.; et al. Novel and efficient synthesis of Ag-ZnO nanoparticles for the sunlight-induced photocatalytic degradation. *Appl. Surf. Sci.* **2019**, *476*, 632−40.
(52) Pedro, A. C.; Paniz, O. G.; Fernandes, I. D. A. A.; Bortolini, D. G.; Rubio, F. T. V.; Haminiuk, C. W. I.; et al. The Importance of Antioxidant Biomaterials in Human Health and Technological Innovation: A Review. *Antioxidants* **2022**, *11*, 1644.
(53) Yiu, H. H.; Niu, H. J.; Biermans, E.; Van Tendeloo, G.; Rosseinsky, M. J. Designed multifunctional nanocomposites for biomedical applications. *Adv. Funct. Mater.* **2010**, *20*, 1599−1609.
(54) Islam, S.; Thangadurai, D.; Adetunji, C. O.; Micheal, O. S.; Nwankwo, W.; Kadiri, O.; et al. Nanomaterials: Applications in Biomedicine and Biotechnology. *Handb Nanomater Nanocomposites Energy Environ. Appl.* **2020**, 1−18.

https://doi.org/10.1021/acsomega.4c08896
ACS Omega 2025, 10, 11948−11960

(55) Zheng, L.; Lin, L.; Su, G.; Zhao, Q.; Zhao, M. Pitfalls of using 1,1-diphenyl-2-picrylhydrazyl (DPPH) assay to assess the radical scavenging activity of peptides: Its susceptibility to interference and low reactivity towards peptides. *Food Res. Int.* **2015**, *76*, 359−65.
(56) Gulcin, İ; Alwasel, S. H. DPPH Radical Scavenging Assay. *Processes* **2023**, *11*, 2248.
(57) Chandrasekar, D.; Madhusudhana, K.; Ramakrishna, S.; Diwan, P. V. Determination of DPPH free radical scavenging activity by reversed-phase HPLC: A sensitive screening method for polyherbal formulations. *J. Pharm. Biomed Anal* **2006**, *40*, 460−4.
(58) Timoshnikov, V. A.; Kobzeva, T. V.; Polyakov, N. E.; Kontoghiorghes, G. J. Inhibition of Fe2+- and Fe3+- induced hydroxyl radical production by the iron-chelating drug deferiprone. *Free Radic Biol. Med.* **2015**, *78*, 118−22.
(59) Chen, L.; Lin, Z.; Liu, L.; Zhang, X.; Shi, W.; Ge, D.; et al. Fe2+/Fe3+ Ions Chelated with Ultrasmall Polydopamine Nanoparticles Induce Ferroptosis for Cancer Therapy. *ACS Biomater Sci. Eng.* **2019**, *5*, 4861−9.
(60) Wang, J.; Ding, H.; Zhu, Y.; Liu, Y.; Yu, M.; Cai, H.; et al. Iron-siRNA Nanohybrids for Enhanced Chemodynamic Therapy via Ferritin Heavy Chain Downregulation. *Angew. Chemie - Int. Ed* **2023**, *62*, 62.
(61) Mohanty, A.; Parida, A.; Raut, R. K.; Behera, R. K. Ferritin: A Promising Nanoreactor and Nanocarrier for Bionanotechnology. *ACS Bio Med. Chem. Au* **2022**, *2*, 258−81.

https://doi.org/10.1021/acsomega.4c08896
ACS Omega 2025, 10, 11948−11960